ADVANCED FUNCTIONAL MATERIALS
www.afm-journal.de

www.MaterialsViews.com

Strain Tuning and Strong Enhancement of Ionic Conductivity in $SrZrO_3$–RE_2O_3 (RE = Sm, Eu, Gd, Dy, and Er) Nanocomposite Films

*Shinbuhm Lee, Wenrui Zhang, Fauzia Khatkhatay, Quanxi Jia, Haiyan Wang, and Judith L. MacManus-Driscoll**

Fast ion transport channels at interfaces in thin films have attracted great attention due to a range of potential applications for energy materials and devices, for, solid oxide fuel cells, sensors, and memories. Here, it is shown that in vertical nanocomposite heteroepitaxial films of $SrZrO_3$–RE_2O_3 (RE = Sm, Eu, Gd, Dy, and Er) the ionic conductivity of the composite can be tuned and strongly enhanced using embedded, stiff, and vertical nanopillars of RE_2O_3. With increasing lattice constant of RE_2O_3 from Er_2O_3 to Sm_2O_3, it is found that the tensile strain in the $SrZrO_3$ increases proportionately, and the ionic conductivity of the composite increases accordingly, by an order of magnitude. The results here conclusively show, for the first time, that strain in films can be effectively used to tune the ionic conductivity of the materials.

1. Introduction

Fast ion transport in planar and vertically aligned interfaces in nanocomposite heteroepitaxial oxide films (hereinafter, nanoscaffold films) have attracted great attention due to potential applications for energy materials and devices.[1–11] Structural incompatibility of the oxides at these interfaces leads both to strain and misfit dislocation formation,[1–11] both of which could enhance the ionic conduction. In $BiFeO_3$–$CoFe_2O_4$ nanoscaffold films,[5,6] a nanoscopic study using scanning probe microscopy revealed spatially localized ion transport at the vertical interfaces. More recently, electric control of the local conduction at vertical interfaces was also demonstrated in $BiFeO_3$–$CoFe_2O_4$[6] and $SrTiO_3$–Sm_2O_3[8] nanoscaffold films.

Strain, in particular tensile strain, has been shown to enhance oxygen ionic conductivity in lateral multilayer systems.[3,4,9–11] The tensile strain reduces the activation energy for oxygen vacancy migration because the spatial volume of the moving species increases.[12] In a lateral multilayer system composed of Y-stabilized ZrO_2 (YSZ) and RE_2O_3 (RE = Y, Lu, and Sc), the ionic conductivity changed systematically depending on the strain state of the YSZ induced by the RE_2O_3 layers.[9,11] Interestingly, ionic conductivity in YSZ/Y_2O_3 multilayers increased by a few orders of magnitude, compared with bulk YSZ film, due to very large tensile strain of 3% in YSZ layer induced by Y_2O_3 layer.

To date few systematic studies have been done to show how ionic conductivity scales with strain.[9–11] Owing to limitations on the availability of single crystal substrates and the difficulty of probing buried planar interfaces, the influence of strain alone on the ionic conduction cannot be easily investigated in standard planar structures. Hence, controversy remains over the true origin of the enhanced ionic conduction at interfaces. Further complications in understanding arise because space charge effects and reconstruction (i.e., formation of interface defects such as dislocations and oxygen vacancies), can also contribute to the enhanced ionic conductivity.[3,4]

In vertical nanoscaffold films, the strain is controlled in the out-of-plane direction because vertical heteroepitaxial matching occurs between two epitaxial oxides within the film, instead of between the film and substrate in the standard planar film case.[8,13–19] Hence, nanoscaffold films offer the following advantages over planar films:

a. By choosing the appropriate two phases in a nanoscaffold film, one phase in the film will act as a stiff, strain-controlling phase, while the other phase (which forms the matrix) will be strain-controlled.[8,13–19] Hence, by using different second phase materials to systematically control the strain, there is the possibility to understand the role of strain independent of the influences of charge and surface reconstruction effects.
b. Since the lateral dimensions of the two phases in the film are only tens of nm, vertical strains of more than 2% can be induced, independent of film thickness.[16,17] Also, the vertical strain remains in much thicker films and is independent of the substrate (when the film thickness is larger than a critical film thickness), which is not the case of standard planar films,

Dr. S. Lee, Prof. J. L. MacManus-Driscoll
Department of Materials Science and Metallurgy
University of Cambridge
27 Charles Babbage Road, Cambridge CB3 0FS, UK
E-mail: jld35@cam.ac.uk
W. Zhang, F. Khatkhatay, Prof. H. Wang
Department of Electrical and Computer Engineering
Texas A&M University
College Station, TX 77843, USA
Dr. Q. Jia
Center for Integrated Nanotechnologies
Los Alamos National Laboratory
Los Alamos, NM 87545, USA

DOI: 10.1002/adfm.201404420

Table 1. Lattice parameters and tensile strain in $SrZrO_3$ in 1 μm thick $SrZrO_3$–RE_2O_3 nanoscaffold films.

		Nanoscaffold film		
	Lattice constant in bulk [Å] a_{bulk}	Measured lattice constant of $SrZrO_3$ [Å] $c_{film}^{SrZrO_3}$	Measured out-of-plane strain in $SrZrO_3$ [%]	Calculated out-of-plane interfacial strain [%]
$SrZrO_3$ ($Pm\bar{3}m$)	4.09 (PDF#760167)	4.11 (pure $SrZrO_3$ film)	$= \frac{c_{film}^{SrZrO_3} - a_{bulk}^{SrZrO_3}}{a_{bulk}^{SrZrO_3}}$	$= \frac{c_{film}^{SrZrO_3} - a_{bulk}^{RE_2O_3}/2\sqrt{2}}{c_{film}^{SrZrO_3}}$
Er_2O_3 ($Ia\bar{3}$)	10.55 (#770459)	4.11	0.05	9.25
Dy_2O_3 ($Ia\bar{3}$)	10.67 (#861327)	4.14	0.6	8.88
Gd_2O_3 ($Ia\bar{3}$)	10.80 (#862477)	4.15	0.9	7.99
Eu_2O_3 ($Ia\bar{3}$)	10.85 (#862476)	4.16	1.1	7.79
Sm_2O_3 ($Ia\bar{3}$)	10.92 (#862479)	4.17	1.3	7.41

PDF: Powder diffraction file (International Center for Diffraction Data).

where strain relaxation occurs after only a few tens of nm film thickness.

c. Crystallinity does not degrade with film thickness which is not the case for standard planar films.[16,17]
d. Ionic conduction occurs perpendicular to the substrate plane, which is what is required for practical devices.
e. Since films can be made thick, >1 μm thickness (while still maintaining strain control),[16,17] they can easily be made structurally rigid and dense.

In this work, we systematically vary strain in relatively thick films by creating nanoscaffold composites $SrZrO_3$–RE_2O_3, incorporating an ionic conducting phase $SrZrO_3$ and second phase RE_2O_3 (RE = Sm, Eu, Gd, Dy, and Er). The $SrZrO_3$–RE_2O_3 nanoscaffold films are ideal for exploring the role of strain since the strain can be systematically changed using different REs. The RE_2O_3 has a cubic bixbyte structure ($Ia\bar{3}$ in space group) and the lattice size depends on the RE. The lattice constant of bulk RE_2O_3 increases from 10.54 (Er_2O_3) to 10.93 Å (Sm_2O_3), as summarized in **Table 1**. $SrZrO_3$ was explored as the ionic conducting material for this study since it is a perovskite and grows well on standard perovskite single crystal substrates, e.g., on $SrTiO_3$. $SrZrO_3$ is a widely used ionic (either proton or oxygen ion) conductor,[20–23] which normally has a high operating temperature above 1000 °C.

We observed very high and strain-tuned ionic conductivity in the composite through varying the second RE_2O_3 phases in the nanoscaffold films. Furthermore, the ion conductivity increased by one order of magnitude by varying RE_2O_3 from Er_2O_3 to Sm_2O_3 with increasing tensile stress in the $SrZrO_3$ from 0.05% to 1.3%.

2. Results and Discussion

Figure 1a shows a schematic cross-sectional image of $SrZrO_3$–RE_2O_3 nanoscaffold film. The $SrZrO_3$ and RE_2O_3 phases spontaneously phase-separate in the nanoscaffold films grown by pulsed laser deposition from a mixed polycrystalline target of $SrZrO_3$ and RE_2O_3. Using cross-sectional view in transmission electron microscopy (TEM) (Figure 1b), we observed nanocolumns of the individual phases of $SrZrO_3$–Sm_2O_3 nanoscaffold film. The stripe patterns perpendicular to the [001] direction are due to the structure of Sm_2O_3 ($Ia\bar{3}$ in space group), which has a different cubic structure from perovskite $SrZrO_3$ ($Pm\bar{3}m$ space group). The stripe patterns are observed more clearly in high-resolution image, as shown in Figure 1c. The vertical interfaces between $SrZrO_3$ and Sm_2O_3 are very sharp, similar to the case for $SrTiO_3$–Sm_2O_3[8] and $BaTiO_3$–Sm_2O_3[16] nanoscaffold films, indicating negligible interface reaction and minimal intermixing between $SrZrO_3$ and Sm_2O_3. The selected area diffraction pattern (inset in Figure 1b) indicates that $SrZrO_3$ has a good cube-on-cube growth on $SrTiO_3$ substrates showing that the $SrZrO_3$–RE_2O_3 nanoscaffold films are highly epitaxial without any high angle grain boundaries. The regular square array of diffraction spots is also evidence that the interfaces in Figure 1b are low angle heteroepitaxial domain boundaries.

When different atom species arrive at the substrate surface simultaneously, surface diffusion will drive the agglomeration of the same species (e.g., $SrZrO_3$ and RE_2O_3). Nucleation occurs in accordance with the minimization of the surface free energy.[19,24] The $SrZrO_3$ phase nucleates more readily on the same-structured perovskite single crystal than does Sm_2O_3, and thus forms the matrix phase, while the Sm_2O_3 phase forms smaller and interspersed columnar islands.[8,13–19] From plan view TEM images (Figure 1d), we found ≈30 nm diameter nanocolumns of Sm_2O_3, which are uniformly distributed in the $SrZrO_3$ matrix. The well-defined interfaces between the nanocolumns and the matrix unambiguously demonstrate clear phase separation of $SrZrO_3$ and Sm_2O_3.

Using Bragg Bretano θ–2θ X-ray diffraction scans, we also confirmed macroscopic phase separation of $SrZrO_3$ and RE_2O_3. Diffraction peaks corresponding only to (00l) $SrZrO_3$ and (00l) RE_2O_3 were observed without any impurity peaks or solid-solution phases, also supporting separation of $SrZrO_3$ and RE_2O_3 and their epitaxial growth. The microstructures and epitaxial quality are broadly the same across the series. From X-ray diffraction ϕ-scans, the in-plane orientation of $SrZrO_3$ was found to be ⟨100⟩ $SrZrO_3$ ‖ ⟨100⟩$SrTiO_3$ and for the RE_2O_3 was found to be ⟨100⟩RE_2O_3 ‖ ⟨110⟩$SrTiO_3$. Considering the lattice constants of RE_2O_3 in the bulk (Table 1), to minimize lattice mismatch, it is very natural that the RE_2O_3 phase grows epitaxially on the Nb-doped $SrTiO_3$ substrate with a 45° in-plane rotation.[8,16,17]

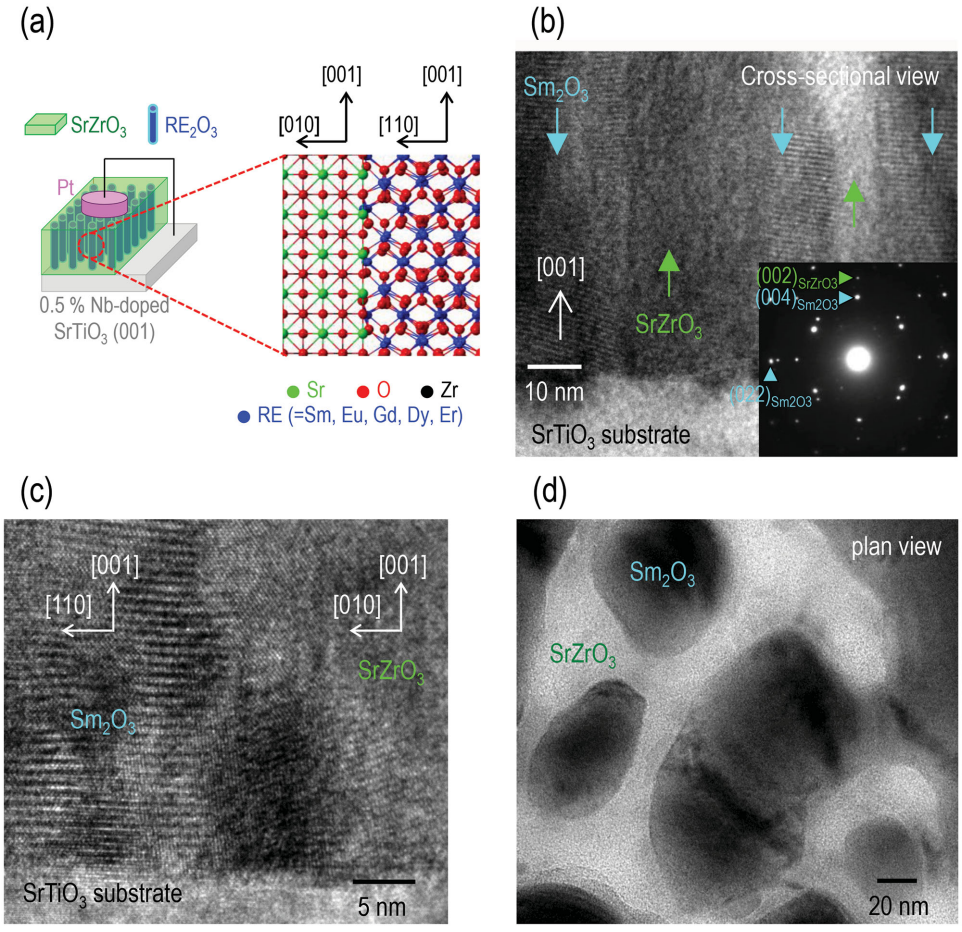

Figure 1. a) Cross-sectional schematic of $SrZrO_3$–RE_2O_3 (RE = Sm, Eu, Gd, Dy, and Er) nanoscaffold films. b) Vertical nanocomposite structure of $SrZrO_3$–Sm_2O_3 films observed by cross-sectional view in TEM. The inset shows a selected area diffraction pattern taken from the film region of the TEM image. c) Clear stripe patterns in Sm_2O_3 phase in high-resolution TEM image. d) Very sharp interfaces are observed between $SrZrO_3$ and Sm_2O_3, as shown in plan view TEM image.

To investigate the strain state of $SrZrO_3$ in the in-plane and out-of-plane directions we took reciprocal space maps about the $(\bar{1}03)$ $SrTiO_3$ substrate for 1 µm thick $SrZrO_3$ in a nanoscaffold film (left in **Figure 2**a) and in a pure film (right). The $SrZrO_3$ peak in the composite sample is skewed in the direction perpendicular to the substrate. This is likely to arise from strain coupling between $SrZrO_3$ and RE_2O_3 and is a common feature of nanocomposite films.[8,16,17] On the other hand, the $SrZrO_3$ peak in the pure film is unskewed since the film is relaxed, giving the bulk lattice parameter of 4.11 Å (see Table 1). Hence, the substrate-induced strain arising from the 5% lattice mismatch between $SrZrO_3$ film and the Nb-doped $SrTiO_3$ substrate does not dominate the strain state in the vertically aligned scaffold films. The $(\bar{1}03)$ $SrZrO_3$ peak in the nanoscaffold film is sharper in the q_z-direction than in the pure film, indicating small spread of the *c*-axis lattice parameters. Hence, little or no strain relaxation through the thickness of the film occurs, again consistent with our earlier studies.[8,16,17]

The $(\bar{1}03)$ $SrZrO_3$ peak in the nanoscaffold film was shifted to a lower value of q_z, compared with the same peak in the pure film. This shift indicates a 1.3% out-of-plane tensile stress and enhanced *c*-axis lattice constant of $SrZrO_3$ in the composite film compared to the bulk value.

We investigated the shift of the $SrZrO_3$ (002) peak position in the X-ray diffraction θ– 2θ scan for different $SrZrO_3$–RE_2O_3 (RE = Sm, Eu, Gd, Dy, and Er) nanoscaffold films of around 1 µm thickness. In a pure $SrZrO_3$ film (left of Figure 2b), a peak of $SrZrO_3$ (002) is observed at $2\theta = 44.0°$, similar to that of bulk $SrZrO_3$. In $SrZrO_3$–Sm_2O_3 nanoscaffold films, the peak was shifted to a smaller angle in 2θ (left of Figure 2a), consistent with the increased out-of-plane tensile strain observed in the reciprocal space maps. The $SrZrO_3$ (002) peak further shifts downward to lower 2θ-values, i.e., to a greater level of tensile strain and increased lattice parameter of the $SrZrO_3$, with increasing lattice parameters of the RE_2O_3 (right in Figure 2b and Table 1). The out-of-plane tensile strain in the $SrZrO_3$ was maximized to 1.3% with Sm_2O_3 and was negligible with Er_2O_3.

To investigate the tensile strain dependence of ionic conductivity, we measured the ac conductivity in $SrZrO_3$–RE_2O_3 nanoscaffold films. After we measured the ac conductance G_{ac}, we calculated σ_{ac} using $\sigma_{ac} = G_{ac}\frac{l}{A}$, where l and A represent film thickness and electrode area, respectively. **Figure 3**a,b shows the frequency *f*-dependence of ac conductivity σ_{ac} and capacitance

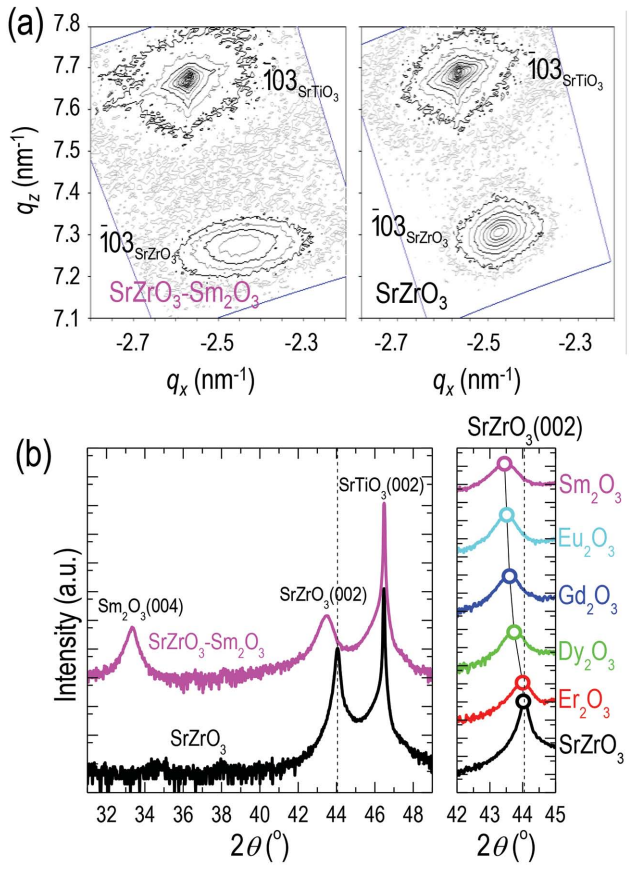

Figure 2. Vertical interface induced tensile strain in $SrZrO_3$ for the $SrZrO_3$–RE_2O_3 nanoscaffold films. a) Reciprocal space mapping about the ($\bar{1}03$) of $SrZrO_3$–Sm_2O_3 nanoscaffold film (left) and pure $SrZrO_3$ film (right). b) X-ray diffraction $\theta - 2\theta$ scans for $SrZrO_3$–Sm_2O_3 nanoscaffold film and pure $SrZrO_3$ film (left). Peak shift of (002) $SrZrO_3$ in X-ray diffraction $\theta - 2\theta$ scans for different $SrZrO_3$–RE_2O_3 (RE = Sm, Eu, Gd, Dy, and Er) nanoscaffold films (right).

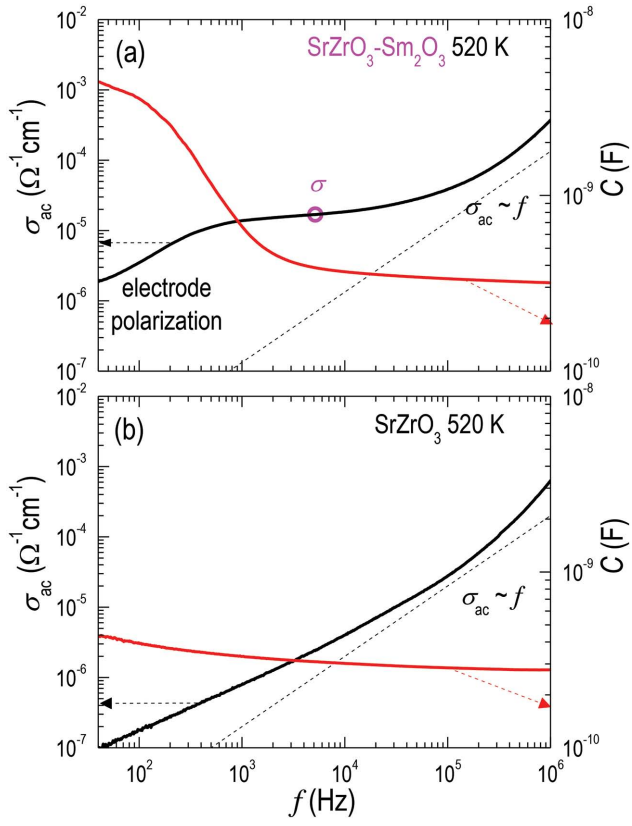

Figure 3. Ionic conductivity and capacitance at 520 K in a) $SrZrO_3$–Sm_2O_3 nanoscaffold film and b) $SrZrO_3$ film. The dashed line represents the linear relationship of $\sigma_{ac} - f$.

C in $SrZrO_3$–Sm_2O_3 nanoscaffold film and $SrZrO_3$ film, respectively, in the f-range of 10–10^6 Hz. At high frequency, σ_{ac} in the $SrZrO_3$–Sm_2O_3 nanoscaffold film decreases with decreasing f (i.e., $\sigma_{ac} \sim f$) since the transport is governed by ion movement in the bulk of the solid electrolyte.[25] At intermediate frequency, the σ_{ac} is independent of f. At low frequency, σ_{ac} decreases again with decreasing f since the ions are blocked by the electrodes and accumulated there (electrode polarization effect).[25] On the other hand, in pure $SrZrO_3$ films, σ_{ac} decreases for the whole f-range without an abrupt change in C. This distinguishable difference of $\sigma_{ac} - f$ indicates that ion transport in $SrZrO_3$–Sm_2O_3 nanoscaffold films is much faster than in the pure $SrZrO_3$ films.

At each temperature, we define ionic conductivity σ from the plateaus of σ_{ac} (circles in Figure 3a). The σ of $SrZrO_3$-RE_2O_3 (RE = Sm, Eu, Gd, Dy, and Er) nanoscaffold films increases with increase of tensile strain for the whole temperature range of 400–800 K (**Figure 4**a).

Pure $SrZrO_3$ films showed negligible ionic conductivity for the whole temperature range studied (400–800 K) and hence is not shown on the plot. Instead, we have included, for comparison, the ionic conductivity of a pure bulk $SrZrO_3$, experimentally reported in the literature.[20] The data are in agreement with the very low ionic conductivity we obtained in our pure $SrZrO_3$ films. We also include the data of 5% mol. Gd-doped $SrZrO_3$ bulk for comparison.[23] It should be noted that the lattice constant of 5% mol. Gd-doped $SrZrO_3$ bulk is 4.11 Å,[23] i.e., the same as the bulk value, indicating that the $SrZrO_3$ lattice was not strained to any measurable extent by Gd-rare earth substitution.

We found that the ionic conductivity in the $SrZrO_3$–Gd_2O_3 nanoscaffold films was higher than that in 5% mol Gd-doped $SrZrO_3$ bulk by almost one order of magnitude. While the ionic conductivity of bulk $SrZrO_3$ increases with Gd doping because the concentration of oxygen vacancies is governed mainly by concentration of the lower-valent dopant in the crystal (e.g., +3 rare earth dopant substituting for Zr^{+4}),[23] our results indicate that the ionic conductivity in the composite films is further increased because of the vertical strain. The different activation energies for ionic conduction of the nanoscaffold strained films (0.8 ± 0.1 eV across the series, cf. 1.1 ± 0.1 eV for Gd-substituted $SrZrO_3$) also prove that the strain dominates the ionic conduction rather than the chemical substitution.

For the nanoscaffold samples, at temperatures below 600 K the ionic conductivity is even higher than for standard YSZ films. It is also interesting that the scaffold sample with the lowest level of strain, namely, $SrZrO_3$–Er_2O_3 (0.05% strain

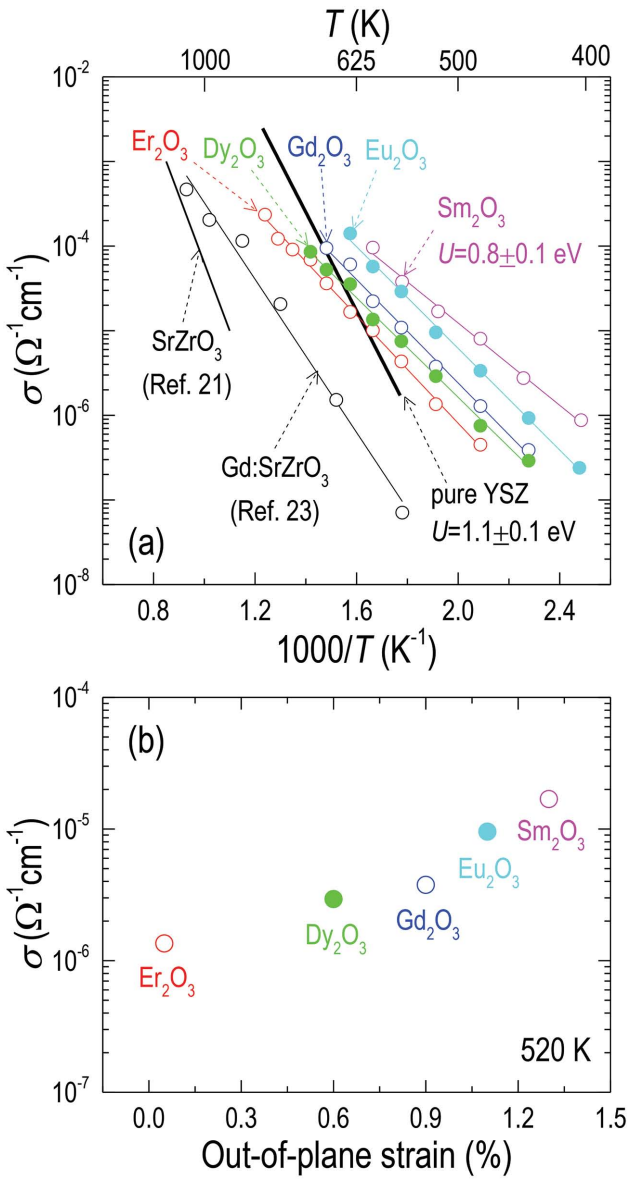

Figure 4. a) Ionic conductivity in $SrZrO_3$–RE_2O_3 nanoscaffold films in temperature range of 400–800 K. For comparison, we include the ionic conductivity data of pure $SrZrO_3$ (ref. [21]) and 5% mol Gd-doped $SrZrO_3$ (ref. [23]) bulk. To obtain the activation energy, we fitted the data using the Arrhenius equation: $\sigma \propto \exp(-E_a/k_BT)$, where k_B denotes the Boltzmann constant. The activation energy E_a is 0.8 ± 0.1 eV for $SrZrO_3$–RE_2O_3 nanoscaffold film, much smaller than 1.1 ± 0.1 eV in pure $SrZrO_3$, 5% mol. Gd-doped $SrZrO_3$ and Y-stabilized ZrO_2 (YSZ). b) Ionic conductivity versus 'out-of-plane' strain in $SrZrO_3$ for the different RE_2O_3 phases in the composite films.

level), still has an ionic conductivity much higher than unstrained Gd-substituted $SrZrO_3$ bulk (e.g., at 625 K, the comparative σ values are 2×10^{-5} and 10^{-6} Ω^{-1} cm^{-1}, respectively). This result suggests that in addition to any RE substitution within the $SrZrO_3$ columns, the structurally misfit heterointerfaces between the $SrZrO_3$ matrix and the RE_2O_3 nanocolumns may contribute to the enhanced conduction, as shown in the earlier works in $BiFeO_3$–$CoFe_2O_4$,[5,6] YSZ-Gd-doped CeO_2,[7] and $SrTiO_3$–Sm_2O_3 nanoscaffold films.[8] It should be noted that the structural change at the interface will not be restricted to one or two atomic layers.[26] However, if we consider the variation of ionic conductivity with strain, both within the $SrZrO_3$ matrix and at the interfacial regions with the RE_2O_3 columns, as calculated in Table 1, we find that while the strain within the $SrZrO_3$ matrix increases systematically with RE_2O_3 lattice size, that strain at the vertical interfaces between the $SrZrO_3$ matrix and the columns, although high, decreases with lattice size. This result indicates that the ionic conduction is dominated by conduction within the $SrZrO_3$ matrix and that it increases with strain within it. It is not surprising that the matrix dominates the ionic conduction over the vertical boundary/interfacial regions since it has a much larger cross-sectional area.

Finally, Figure 4b shows σ versus out-of-plane strain in the $SrZrO_3$ films with different RE_2O_3 nanocolumns. We see that σ in the tensile-strained $SrZrO_3$–Sm_2O_3 nanoscaffold films is higher than in nonstrained $SrZrO_3$–Er_2O_3 nanoscaffold films by almost one order of magnitude (Figure 4b). Also, there is a systematic increase in σ with out-of-plane strain, thus clearly proving the role of strain in enhancing ionic conduction in this system. The σ reaches 10^{-4} Ω^{-1} cm^{-1} near 600 and 750 K in $SrZrO_3$–Sm_2O_3 and $SrZrO_3$–Er_2O_3 nanoscaffold films, respectively. Therefore, by increasing the tensile strain by 1.3% (Table 1) the operation temperature of the $SrZrO_3$ is reduced by almost 150 K. To determine whether our experimental data are consistent with the theoretical predictions, we consider recent calculations of how the ratio of ionic conductivities for strained and nonstrained films varies with the level of epitaxial strain $\Delta a/a$. It is found that

$$\ln\left(\frac{\sigma_{\text{strained}}}{\sigma_{\text{non-strained}}}\right) \cong \frac{1}{3}\frac{\Delta V^M}{RT}\frac{Y}{1-\nu}\frac{\Delta a}{a} \quad (1)$$

where a represents the lattice constant in nonstrained film.[9–11] The Δa is defined as the difference of lattice constants for strained and nonstrained films. ΔV^M, Y (≈250 GPa), and ν (≈0.261) represent the volume of migration of oxygen vacancies, the Young's modulus, and the Poisson ratio of $SrZrO_3$, respectively.[27] Although the ΔV^M-value for $SrZrO_3$ is not known here, we would expect that $\frac{\sigma_{\text{strained}}}{\sigma_{\text{non-strained}}}$ increases with $\Delta a/a$ from Equation (1). That is, in our experiments of $SrZrO_3$–RE_2O_3 nanoscaffold films, $\frac{\sigma_{\text{strained}}}{\sigma_{\text{non-strained}}} \approx 10$ when $\Delta a/a \cong 0.013$. For comparison, widely studied YSZ materials ($\Delta V^M \approx 2.08 \times 10^{-6}$ m^3 mol^{-1}, $Y \approx 180$ GPa, and $\nu \approx 0.3$) were considered.[9,11] In lateral multilayer thin film of YSZ and Y_2O_3, $\frac{\sigma_{\text{strained}}}{\sigma_{\text{non-strained}}} \approx 2.7$ when $\Delta a/a \cong 0.03$.[9] In lateral multilayer thin film of YSZ and Sm-doped CeO_2, $\frac{\sigma_{\text{strained}}}{\sigma_{\text{non-strained}}} \approx 16$ when $\Delta a/a \cong 0.06$.[28] Our experimental data showing a reduction in operation temperature by 150 K for a 1.3% tensile strain level is consistent with both of the above examples for YSZ-based multilayers.

3. Conclusion

Vertical nanoscaffold films of $SrZrO_3$–RE_2O_3 were explored to study and tune the oxygen ionic conductivity in $SrZrO_3$. A

strong tensile strain was generated in the $SrZrO_3$ matrix using vertical nanoscaffold columns of RE_2O_3. The ionic conductivity was observed to increase with tensile strain in the $SrZrO_3$, induced by increasing the lattice mismatch strain by using different RE_2O_3 (RE = Sm, Eu, Gd, Dy, and Er). The ionic conductivity in tensile-strained $SrZrO_3$–Sm_2O_3 nanoscaffold films is larger than that in nonstrained $SrZrO_3$–Er_2O_3 nanoscaffold films by almost one order of magnitude, and is higher than in bulk $SrZrO_3$ by several orders of magnitude. Our results show that ionic conductivity in $SrZrO_3$ is tuned by strain. Our nanocomposite films are effective for creating strongly enhanced ionic conducting channels in the desired perpendicular to film-plane direction.

4. Experimental Section

Insulating $SrZrO_3$–RE_2O_3 (RE = Sm, Eu, Gd, Dy, and Er) nanoscaffold films were deposited onto 1 at% Nb-doped $SrTiO_3$ (001) substrates by pulsed laser deposition. A polycrystalline target containing 50:50 wt% mix of $SrZrO_3$ and RE_2O_3 was used. A KrF laser ($\lambda = 248$ nm) with a fluence of 1.5 J cm^{-2} and a repetition rate of 1 Hz was used. The films were grown at a substrate temperature of 800 °C and an oxygen pressure of 0.2 mbar. The samples were postannealed at 650 °C for 1 h under 400 mbar O_2 to assure proper oxygen stoichiometry and minimize the creation of oxygen vacancy inside films. Nb-doped STO (001) single crystal was selected as the substrate since it has been considered as a solid oxide fuel cell anode material due to redox stability and electrochemical properties.[29,30] Circular Pt electrodes of 50 μm radius defined by shadow masks were deposited by DC magnetron sputtering onto the $SrZrO_3$–RE_2O_3 nanoscaffold films. Plain $SrZrO_3$ and RE_2O_3 films were fabricated under the same deposition procedure using $SrZrO_3$ and RE_2O_3 polycrystalline targets, respectively. X-ray diffraction was carried out with a Panalytical Empyrean high-resolution X-ray diffractometer using Cu-Kα radiation ($\lambda = 1.5405$ Å).

Microstructural characterization was conducted using TEM (FEI Tecnai G2 F20) operated at 200 kV. Cross-sectional samples for TEM characterization were prepared by a standard manual grinding and thinning of samples with a final ion-milling step (Gatan PIPS 691 precision ion polishing system).

To measure the transport characteristics of the samples with temperature, samples were heated on a hot plate, from 20 to 550 °C, and used a probe station equipped with an HP 4294A Precision Impedance Analyzer to measure the ac impedance spectra. For all electrical measurements, the Nb-doped $SrTiO_3$ substrate was grounded and the voltage was applied to the Pt electrodes.

Acknowledgements

This work was supported by the European Research Council (ERC) (Advanced Investigator Grant No. ERC-2009-AdG-247276-NOVOX), the UK Engineering and Physical Sciences Research Council (EPSRC), and the U.S. National Science Foundation (Grant No. DMR-1401266). The work at Los Alamos was partially supported by the NNSA's Laboratory Directed Research and Development Program and was performed, in part, at the Center for Integrated Nanotechnologies, an Office of Science User Facility operated for the U.S. Department of Energy (DOE) Office of Science.

Received: December 13, 2014
Revised: April 15, 2015
Published online: June 5, 2015

[1] J. Garcia-Barriocanal, A. Rivera-Calzada, M. Varela, Z. Sefrioui, E. Iborra, C. Leon, S. J. Pennycook, J. Santamaria, *Science* **2008**, *321*, 676.
[2] T. J. Pennycook, M. J. Beck, K. Varga, M. Varela, S. J. Pennycook, S. T. Pantelides, *Phys. Rev. Lett.* **2010**, *104*, 115901.
[3] C. Leon, J. Santamaria, B. A. Boukamp, *MRS Bull.* **2013**, *38*, 1056.
[4] B. Yildiz, *MRS Bull.* **2014**, *39*, 147.
[5] Y.-H. Hsieh, J.-M. Liou, B.-C. Huang, C.-W. Liang, Q. He, Q. Zhan, Y.-P. Chiu, Y.-C. Chen, Y.-H. Chu, *Adv. Mater.* **2012**, *24*, 4564.
[6] Y.-H. Hsieh, E. Strelcov, J.-M. Liou, C.-Y. Shen, Y.-C. Chen, S. V. Kalinin, Y.-H. Chu, *ACS Nano* **2013**, *7*, 8627.
[7] Q. Su, D. Yoon, A. Chen, F. Khatkhatay, A. Manthiram, H. Wang, *J. Power Sources* **2013**, *242*, 455.
[8] S. Lee, A. Sangle, P. Lu, A. Chen, W. Zhang, J. S. Lee, H. Wang, Q. X. Jia, J. L. MacManus-Driscoll, *Adv. Mater.* **2014**, *26*, 6284.
[9] N. Schichtel, C. Korte, D. Hesse, J. Janeka, *Phys. Chem. Chem. Phys.* **2009**, *11*, 3043.
[10] N. Schichtel, C. Korte, D. Hesse, N. Zakharov, B. Butz, D. Gerthsen, J. Janek, *Phys. Chem. Chem. Phys.* **2010**, *12*, 14596.
[11] C. Korte, J. Keppner, A. Peters, N. Schichtel, H. Aydin, J. Janek, *Phys. Chem. Chem. Phys.* **2014**, *16*, 24575.
[12] J. Hinterberg, T. Zacherle, R. A. De Souza, *Phys. Rev. Lett.* **2013**, *110*, 205901.
[13] J. L. MacManus-Driscoll, P. Zerrer, H. Wang, H. Yang, J. Yoon, A. Fouchet, R. Yu, M. G. Blamire, Q. X. Jia, *Nat. Mater.* **2008**, *7*, 314.
[14] A. Fouchet, H. Wang, H. Yang, J. Yoon, Q. X. Jia, J. L. MacManus-Driscoll, *IEEE Trans. Ultrason., Ferroelectr., Freq. Control* **2009**, *56*, 1534.
[15] J. L. MacManus-Driscoll, *Adv. Funct. Mater.* **2010**, *20*, 2035.
[16] S. A. Harrington, J. Zhai, S. Denev, V. Gopalan, H. Wang, Z. Bi, S. A. T. Redfern, S.-H. Baek, C. W. Bark, C.-B. Eom, Q. X. Jia, M. E. Vickers, J. L. MacManus-Driscoll, *Nat. Nanotechnol.* **2011**, *6*, 491.
[17] O. J. Lee, S. A. Harrington, A. Kursumovic, E. Defay, H. Wang, Z. Bi, C.-F. Tsai, L. Yan, Q. X. Jia, J. L. MacManus-Driscoll, *Nano Lett.* **2012**, *12*, 4311.
[18] A. Kursumovic, E. Defay, O. J. Lee, C.-F. Tsai, Z. Bi, H. Wang, J. L. MacManus-Driscoll, *Adv. Funct. Mater.* **2013**, *23*, 5881.
[19] A. Chen, Z. Bi, Q. X. Jia, J. L. MacManus-Driscoll, H. Wang, *Acta Mater.* **2013**, *61*, 2783.
[20] H. H. Huang, M. Ishigame, S. Shin, *Solid State Ionics* **1991**, *47*, 251.
[21] J. A. Labrincha, F. M. B. Marques, J. R. Frade, *J. Mater. Sci.* **1995**, *30*, 2785.
[22] H. Iwahara, *Solid State Ionics* **1996**, *86*, 9.
[23] W. Zając, D. Rusinek, K. Zheng, J. Molenda, *Cent. Eur. J. Chem.* **2013**, *11*, 471.
[24] H. Zheng, F. Straub, Q. Zhan, P.-L. Yang, W.-K. Hsieh, F. Zavaliche, Y.-H. Chu, U. Dahmen, R. Ramesh, *Adv. Mater.* **2006**, *18*, 2747.
[25] J. C. Dyre, P. Maass, B. Roling, D. L. Sidebottom, *Rep. Prog. Phys.* **2009**, *72*, 046501.
[26] J. Maier, *Nat. Mater.* **2005**, *4*, 805.
[27] Q.-J. Liu, Z.-T. Liu, L.-P. Feng, H. Tian, *J. Solid State Chem.* **2012**, *196*, 425.
[28] S. Sanna, V. Esposito, A. Tebano, S. Licoccia, E. Traversa, G. Balestrino, *Small* **2010**, *6*, 1863.
[29] P. Blennow, K. K. Hansen, L. R. Wallenberg, M. Mogensen, *Solid State Ionics* **2009**, *180*, 63.
[30] X. Guo, J. Maier, *Adv. Mater.* **2009**, *21*, 2619.